

Complex Refractive Indices of $\text{Cd}_x\text{Zn}_{1-x}\text{O}$ Thin Films Grown by Molecular Beam Epitaxy

J.W. MARES,^{1,3} M. FALANGA,¹ W.R. FOLKS,¹ G. BOREMAN,¹
A. OSINSKY,² B. HERTOOG,² J.Q. XIE,² and W.V. SCHOENFELD¹

1.—CREOL, The College of Optics and Photonics, University of Central Florida, Orlando, FL 32816, USA. 2.—SVT Associates, Inc., Eden Prairie, MN 55344, USA. 3.—e-mail: jmares@mail.ucf.edu

The complex refractive indices of $\text{Cd}_x\text{Zn}_{1-x}\text{O}$ thin films were determined by transmission spectrophotometry. Transmission spectra were modeled from 375 nm to 800 nm for samples having cadmium concentrations ranging from 2% to 77%. The transparent and absorptive regimes were fitted separately by Sellmeier and Forouhi–Bloomer models, respectively. Real refractive indices of $\text{Cd}_x\text{Zn}_{1-x}\text{O}$ shift to higher values in the transparent region and the optical absorption edge shifts to longer wavelengths with increasing cadmium concentration. Spectroscopic ellipsometry was carried out on one sample from $\lambda = 190$ nm to 1.8 μm . Comparison between the two methods shows that the results are in general agreement.

Key words: Ellipsometry, refractive index, optical constants, cadmium zinc oxide, wide-bandgap semiconductors, spectrophotometry

INTRODUCTION

Group II oxide compounds are currently of increasing interest for applications in wide-bandgap optoelectronic devices. In particular, wurtzite ZnO, a material that has found applications in technologies exploiting its piezoelectric and photoelastic properties,^{1–4} has experienced renewed interest for use in semiconductor light emitters and detectors.^{5–9} In recent decades application of this material in such technology has been impeded by the difficulty of achieving the stable *p*-type doping necessary for device engineering.^{10,11} Additionally, the concurrent success of III-nitride-based compounds in realizing efficient blue and ultraviolet devices^{12,13} over the past decade has hindered commercial interest in potential applications of ZnO for such devices. Despite this, interest in ZnO-based semiconductor compounds did not fully diminish because of unique aspects that offer advantages in device functionality as well as device production and integration. High-quality native ZnO substrates are

currently available in large diameters (>50 mm), offering an excellent template for epitaxial growth of device structures.¹⁴ ZnO compounds can be wet etched, even selectively in some cases,¹⁵ which may enable efficient fabrication techniques and novel structures. Furthermore, ZnO has been shown to be radiation hard¹⁰ relative to GaAs and GaN, making it a good platform for use in radiation-intense environments.

The bandgap and optical properties of ZnO ternary alloys are sufficiently variable to facilitate optoelectronic device engineering. Bandgap variation in the material system has been successfully achieved by alloying ZnO with magnesium or beryllium, to shift to higher bandgap energies,^{16–20} or with cadmium to shift to lower energies.^{18,21,22} Optical properties of ZnO are also desirable in that it is transparent in the visible spectrum and has a relatively high refractive index ($n \approx 2.0$ at $\lambda = 600$ nm).^{23–25} Reduction of the refractive index by alloying ZnO with magnesium has already been investigated,^{25–30} as discussed below. In addition, high-quality thin-film ZnO exhibits low loss due to scattering and has therefore been utilized in optical waveguide structures^{31–34} that may find use in

(Received February 25, 2008; accepted July 9, 2008; published online August 19, 2008)

integrated optoelectronic systems. Doped and undoped ZnO films of varying degrees of crystallinity exhibit good conductivity and are well explored for use as transparent conducting oxide (TCO) films.^{35–37} Perhaps the most commonly emphasized semiconductor property of ZnO is its large free-exciton binding energy^{38,39} (~ 60 meV), which is credited as enabling lasing in epitaxial layers at temperatures up to 570 K.⁴⁰ Thus, the persistence in ZnO-related research has occurred not only as a result of improvements in epitaxial growth and engineering methods,^{5–7,9–11,16,21,41–45} but also the continued exploration of its unique material properties.

In order to implement waveguide structures, including both passive waveguides and those used in active devices such as optical confinement double heterostructures, the material's refractive index must be sufficiently variable. As noted, the refractive indices of $\text{Mg}_x\text{Zn}_{1-x}\text{O}$ thin films have been thoroughly characterized over the entire range of magnesium concentration $0 \leq x \leq 1$ and over a broad spectral range.^{26,29,30} In general, there is a decrease in the refractive index of $\text{Mg}_x\text{Zn}_{1-x}\text{O}$ with increasing magnesium incorporation. With Mg concentrations approaching $x \approx 0.5$ to 0.6, however, $\text{Mg}_x\text{Zn}_{1-x}\text{O}$ transitions to the cubic phase,^{25,26,46} thereby precluding wurtzite applications and restricting the applicable range of refractive indices for that compound. For improved confining structures, a greater range of refractive indices is desirable. Because alloying ZnO with cadmium is known to shift the bandgap to lower energies, it is logical to investigate the behavior of the refractive index as it changes with cadmium content. While various techniques exist to characterize refractive indices of thin films, one effective and experimentally simple measurement technique is transmission spectrophotometry.

EXPERIMENTAL

Spectrophotometry and Analysis

Wurtzite $\text{Cd}_x\text{Zn}_{1-x}\text{O}$ samples of varying cadmium concentrations were epitaxially grown by oxygen plasma-assisted molecular beam epitaxy (MBE) on single-side-polished *c*-plane (0001) $\text{Al}_2\text{O}_3/\text{GaN}$ templates as previously described.⁸ Six samples with cadmium contents of $x = 0.02, 0.09, 0.16, 0.30, 0.64,$ and 0.77 were chosen for refractive index characterization. Compositional properties of the thin films were first characterized with Rutherford backscattering (RBS) and secondary-ion mass spectroscopy (SIMS) to provide the relative cadmium concentrations for each sample. The RBS and SIMS depth profiles also revealed abrupt interfaces between successive layers of growth and confirm uniform composition within each layer. Thicknesses of the samples are 200, 175, 225, 200, 415, and 670 nm for $x = 0.02, 0.09, 0.16, 0.30, 0.64,$ and 0.77, respectively. The error in layer thickness

measurements is less than 10 nm. X-ray diffraction (XRD) showed that the films were of the wurtzite structure and did not exhibit any observable cubic phase component.⁸ Photoluminescence (PL) and atomic force microscopy (AFM) were also carried out as previously presented.⁴⁷ In summary, PL results showed behavior that is in general agreement with $\text{Cd}_x\text{Zn}_{1-x}\text{O}$ films grown elsewhere,^{9,42–45} and AFM revealed epitaxially smooth surfaces with root-mean-square (RMS) roughness less than 10 nm for the samples measured (samples available at that time were those for which $x \leq 0.30$).

To enable accurate transmission measurements the sample substrates were polished to optical smoothness to eliminate scattering effects due to the initially rough backside of the sapphire substrates. The samples were polished and smoothed using an Allied wheel polisher with diamond lapping films ranging in grain size from 30 μm to 100 nm. Subsequent comparison of measurements with the theoretical model reveals that losses due to scattering are less than the accuracy of the transmission measurements.

Transmission spectral measurements were taken on the samples using a Varian Cary 500 spectrophotometer over the wavelength range 375–800 nm in 1 nm increments with the bandwidth of measurement set to less than 1 nm/point. Transmission measurements were taken at 0 deg angle of incidence parallel to the crystalline *c*-axis; thus only the ordinary refractive indices were interrogated. A 1-mm-diameter circular aperture was used to laterally restrict the measured region. The measured transmission spectrum of each sample was analyzed using an evolutionary algorithm which employed a transmission-matrix system representation as a means of fitting the dispersion relation to experimental data.

The fitting algorithm used is similar to other implementations found in related multivariable model fitting and optimization problems.^{48–50} The algorithm initiates by posing a set of solutions consisting of dispersion relation parameters in a pre-defined parameter space. The solutions are then evaluated by calculating the point-by-point least-squares difference, χ^2 between the measured spectrum, and the spectrum predicted by the solution

$$\chi^2 = \frac{\sum_j \{T_T(\lambda_j) - T_E(\lambda_j)\}^2}{N}, \quad (1)$$

where N is the number of points, and T_T and T_E are the theoretically predicted and experimentally measured values of transmission, respectively. The transmission-matrix formulation method is used to model the transmission of the multilayer structure. Interfaces are represented by reflection matrices \hat{H}_i , and film layers by propagation matrices \hat{L}_i .

$$\tilde{H}_i = \frac{1}{\tau_i} \begin{bmatrix} 1 & r_i \\ r_i & 1 \end{bmatrix} \quad (2)$$

$$\tilde{L}_i = \begin{bmatrix} e^{i\beta_i} & 0 \\ 0 & e^{-i\beta_i} \end{bmatrix}. \quad (3)$$

Here, τ_i and r_i are the wavelength-dependent Fresnel transmission and reflection coefficients at the interface. Variables η_i are the complex indices of refraction of the layers, and d_i are the layer thicknesses. Propagation constants for the layers, β_i , are given at normal incidence as

$$\beta_i(\lambda) = \frac{2\pi}{\lambda_0} \eta_i(\lambda) d_i. \quad (4)$$

By concatenating matrices, a thin-film structure with an arbitrary number of layers can be represented as a system matrix, from which transmission coefficients T are determined by the equation

$$T = t^2 = \left(\frac{1}{s_{22}} \right)^2. \quad (5)$$

Solutions are ranked in order of decreasing error and are procedurally altered through a pseudorandom parameter perturbation function known as Gaussian mutation.^{51,52} This process is repeated until a minimum error is achieved and a solution is converged upon.

Two optical dispersion models were chosen for their simplicity and applicability. For the transparent regime where the loss is considered negligible ($\kappa \approx 0$) the Sellmeier model is given by

$$n^2(\lambda) = A + \frac{B\lambda^2}{\lambda^2 - C^2}, \quad (6)$$

where A , B , and C are fitting parameters. In the absorbing region at shorter wavelengths the multiple oscillator Forouhi–Bloomer (FB) model is used:

$$n(E) = n(\infty) + \sum_{i=1}^q \frac{B_{0i}E + C_{0i}}{E^2 - B_iE + C_i} \quad (7)$$

$$k(E) = \sum \frac{A_i(E - E_g)^2}{E^2 - B_iE + C_i} \quad (8)$$

in which $n(\infty)$, A_i , B_i , C_i , and E_g are the five fitting parameters, and B_{0i} , C_{0i} , and Q_i are given by

$$B_{0i} = \frac{A_i}{Q_i} \left(-\frac{B_i^2}{2} + E_g B_i - E_g^2 + C_i \right) \quad (9)$$

$$C_{0i} = \frac{A_i}{Q_i} \left((E_g^2 + C_i) \frac{B_i}{2} - 2E_g C_i \right) \quad (10)$$

$$Q_i = \frac{1}{2} (4C_i - B_i^2)^{1/2}. \quad (11)$$

This model is consistent with the Kramers–Kronig relation and has been used to model the refractive indices of various optical materials including both dielectrics and semiconductors.^{53–55} An advantageous property of the FB model is that the imaginary component of index of refraction, and therefore the absorption coefficient, is identically zero at the wavelength value of the bandgap parameter. The first step in analyzing the transmission spectra, therefore, consisted of extending the FB domain (absorptive region) until the zero-absorption point was determined. The data for each sample is then divided at its respective approximate bandgap parameter. The transmission spectra above this energy parameter are treated with the FB model, and the spectra below it are treated with the Sellmeier dispersion model. It is important to note that, while E_g is referred to as the bandgap parameter, this value does not accurately represent the true semiconductor bandgap. This is because absorption occurs at energies below the bandgap due to excitonic absorption²² and band-tailing effects. The model nonetheless remains functional when the bandgap parameters are less than the material bandgap, and the various absorption phenomena are represented by oscillator terms.

Spectroscopic Ellipsometry and Analysis

Spectroscopic ellipsometry was performed on one of the samples to introduce an independent experimental method to verify the modeling results and study in detail some of the subtler features of the spectrum. Spectroscopic ellipsometry is a well-established technique to measure the optical constants of a thin film. There are many texts on the subject that the reader may reference which describe the details of the method.^{56–58} In spectroscopic ellipsometry the change in the polarization state of light is measured after reflection from the sample surface and interfaces. The two key measurement parameters, Ψ and Δ , are related to the change in amplitude and phase shift of the impinging \vec{E} field upon reflection, and are wavelength dependent. These two parameters are fit simultaneously to a generalized oscillator model which assigns an oscillator to each absorption peak in the spectrum. In this measurement our sample was prepared by homogeneously roughening the backside by sandblasting prior to measurement to scatter any light reaching the back surface. This step simplifies modeling nonidealities in the data due to the finite bandwidth of the instrument and thickness nonuniformities of the sample which introduce depolarization of the signal. Additionally, because the sapphire substrate is known to be anisotropic, suppression of the back surface reflection tends to suppress anisotropic effects on the data, further simplifying the modeling process. It is

important to note that the $\text{Cd}_x\text{Zn}_{1-x}\text{O}$, as a wurtzite structure compound, is expected to exhibit birefringence. However, the ellipsometric properties measured on such *C*-plane-oriented samples are dictated by the material's dielectric response in the plane of the sample surface. Thus, the spectroscopic ellipsometry measurements presented here yield the ordinary refractive indices of the films.

Measurements were performed on the 16% sample of $\text{Cd}_x\text{Zn}_{1-x}\text{O}$ at multiple detector angles from 55 deg to 80 deg in 5 deg intervals with a spectral resolution of 16 cm^{-1} ($\sim 1.6\text{ nm}$). Results are presented in Fig. 7. Measurements were performed in standard reflection mode because reflective spectroscopic ellipsometry is known to be more sensitive to absolute values of n and κ compared with measurements performed in transmission mode. As mentioned previously, this allows us to avoid anisotropic effects due to the sapphire substrate which would be introduced if the measurement was done in transmission mode. The data was modeled as a linear superposition of Gaussian oscillators, which is Kramers–Kronig consistent, and where each oscillator represents a unique absorption peak in the spectrum. A Tauc–Lorentz oscillator was used to represent the semiconductor bandgap transition occurring just below the UVA range. Poles were placed outside the data range to account for $n(\infty)$ and surface roughness, and layer thickness nonuniformity were also accounted for in the model. Optical constants n and κ or permittivity values ϵ' and ϵ'' were then extracted.

RESULTS AND DISCUSSION

Spectrophotometry

Measured transmission spectra for $x = 0.02, 0.16, 0.30,$ and 0.77 samples are shown in Fig. 1. Variation of the material bandgap is evidenced by a shift in the optical absorption edge to longer wavelengths for increasing cadmium content. The separation point between absorptive and nonabsorptive regions, as determined by the FB κ minimum point, is indicated by the arrow on each graph. For Fig. 1a–c, note the visibility of two separate absorption edges. The longer wavelength edge is the result of the $\text{Cd}_x\text{Zn}_{1-x}\text{O}$ surface layer; the shorter wavelength edge at approximately 374 nm is due to the underlying ZnO layer. This effect is not seen in Fig. 1d because the $\text{Cd}_x\text{Zn}_{1-x}\text{O}$ layer of this sample is several times thicker than the lower percentage samples and is absorptive in that region. The transmission spectra of the $x = 0.09$ and $x = 0.64$ samples obeyed the trend shown and are omitted to conserve space.

A typical fit achieved by the evolutionary algorithm is shown in Fig. 2. Good agreement in both phase and amplitude of interference fringes suggest accurate application of the model. Note that a slight disagreement exists between the amplitude of the fringes modeled and those measured, primarily

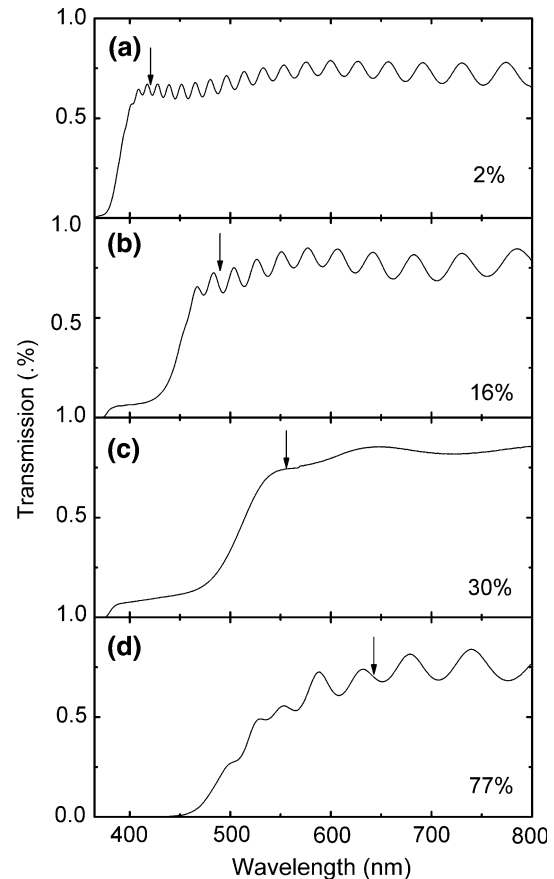


Fig. 1. Transmission curves measured for four $\text{Cd}_x\text{Zn}_{1-x}\text{O}$ samples. The location of the arrow indicates the value at which the transmission spectrum is initially divided between absorptive and transparent regions.

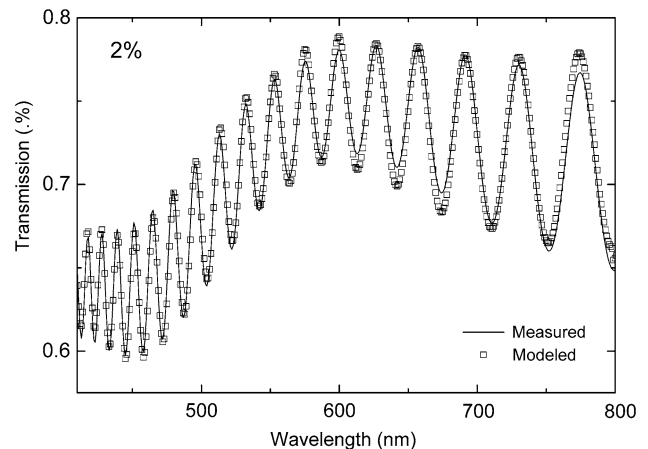


Fig. 2. The experimentally measured and theoretically fit transmission curves for the $x = 0.02$ sample in the transparent region.

above 600 nm. This is a result of assuming zero absorption in the Sellmeier region. In fact, it is expected from photoluminescence measurements that there are deep-level transitions that will allow

absorption in that wavelength range⁴⁷ and these are not accounted for in the index modeling.

The attained fits all satisfied the criteria of $\chi^2 \leq 10^{-4}$ and represent converged solutions. The refractive indices resulting in the best-fit transmission curves in the transparent region are shown in Fig. 3, and the associated parameters are listed in Table I. At $\lambda = 800$ nm the real refractive index is

seen to increase with increasing cadmium concentration from $n = 1.96$ to $n = 2.22$. In addition, the wavelength location of the asymptote in the Sellmeier dispersion relation shifts from $C = 335$ nm to $C = 571$ nm. This parameter shift shows the change in behavior in the normal dispersion regime.

Figure 4 shows the real refractive indices as predicted by the FB model fits in the absorptive region. The associated parameter values are listed in Table I. There is a shift in the refractive index peak from 383 nm to 497 nm for cadmium concentrations of $x = 0.02$ and $x = 0.30$, respectively. These samples also exhibited a general broadening with increasing cadmium concentration. The refractive index at the low-energy edge of the absorptive regions agreed reasonably well with those at the high-energy edge of the transparent region. Continuity between the two regions was not intrinsically enforced in the fitting algorithm and therefore some discontinuities are present. The greatest discontinuity is seen in the dispersion curves of the $x = 0.02$ sample at $\lambda = 415$ nm and the disagreement is approximately $\Delta n = 0.07$. This disagreement is likely due to error in the initial selection of the separation wavelength between the two regions.

The behavior of the $x = 0.64$ and $x = 0.77$ samples do not obey the same overall trend in the peak shift that is observed in the other four samples in the absorptive region. For these two samples, multiple solutions were found which had approximately

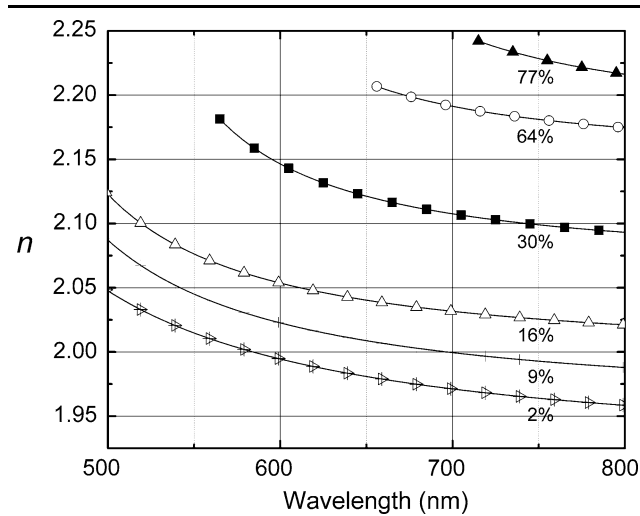


Fig. 3. The real refractive indices for all samples in the transparent region as fit to the Sellmeier optical dispersion model.

Table I. Forouhi–Bloomer and Sellmeier Fitting Parameters and Corresponding Wavelength Ranges for all Samples

Cd (%)	Forouhi–Bloomer						Sellmeier			
	$n(\infty)$	E_g (eV)	A_i	B_i (eV)	C_i (eV ²)	λ (nm)	A	B	C (μ m)	λ (nm)
2	1.530	2.949	0.097	6.596	10.902	375–420	3.118	0.592	0.335	420–800
			0.00004	8.575	23.922					
			0.064	10.105	26.928					
			0.076	13.062	44.02					
9	1.601	2.612	0.099	5.957	8.93	375–474	3.498	0.349	0.385	474–800
			0.016	6.742	11.419					
			0.019	8.687	18.884					
			0.017	11.39	34.521					
16	1.605	2.514	0.086	5.650	8.017	375–493	3.724	0.268	0.405	493–800
			0.095	6.463	10.703					
			0.079	7.880	17.077					
			0.081	12.170	41.687					
30	1.711	2.224	0.186	4.872	6.005	375–557	4.090	0.187	0.480	557–800
			0.080	6.056	9.947					
			0.007	6.972	63.718					
			0.037	11.649	34.141					
64	1.726	1.887	0.010	3.731	3.489	400–657	4.489	0.136	0.525	657–800
			0.052	6.332	10.156					
			0.067	8.116	20.672					
			0.096	10.065	27.203					
77	1.707	1.733	0.007	5.794	8.418	425–715	4.587	0.160	0.571	715–800
			0.074	6.580	11.186					
			0.225	15.240	84.594					
			0.015	12.933	44.936					

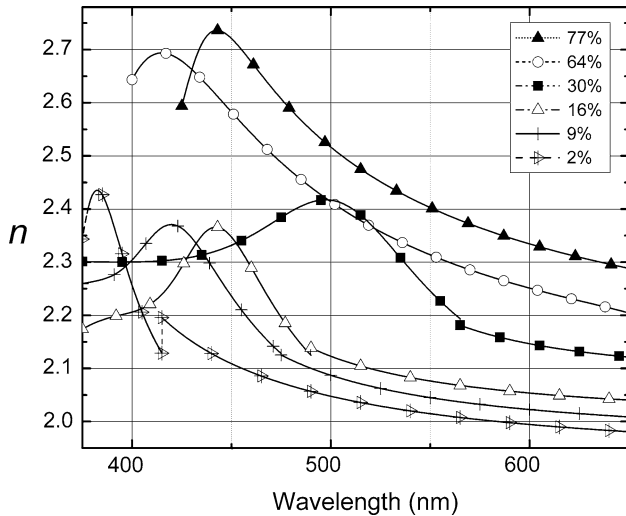


Fig. 4. The real refractive indices for all samples in the absorptive region as fit to the Forouhi–Bloomer optical dispersion model. The FB formulation is extended into the transparent region until $\kappa = 0$ and matched with the Sellmeier model. Strict continuity was not enforced in the fitting algorithm, allowing some discontinuities to exist between absorbing and transparent regions.

equally low error (χ^2), but varied in the location and value of their peaks. Variation in the peak location of approximately 30 nm was observed for the $x = 0.64$ sample and more than 65 nm variation was seen in the $x = 0.77$ peak location. The values of the peaks were observed to vary by more than $\Delta n = 0.2$ for both samples. Curves are included for posterity and the source of such ambiguity is addressed below.

The imaginary part of refractive index is shown in Fig. 5 for the six samples. A shift in the absorption edge to lower energies is observed with increasing cadmium content. Samples with cadmium concen-

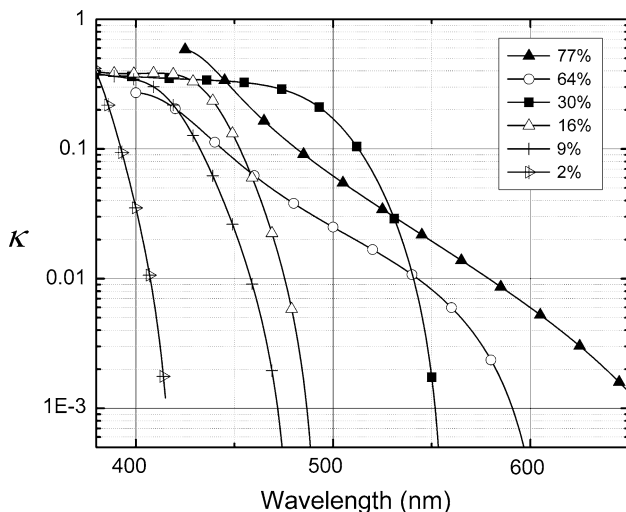


Fig. 5. The imaginary refractive indices for all samples in the absorptive region as fit to the Forouhi–Bloomer optical dispersion model.

trations less than 0.30 show similar behavior and all have a maximum κ value of approximately 0.4. The $x = 0.64$ and $x = 0.77$ samples show much broader absorption edges and reach maximum values of $\kappa = 0.2$ and $\kappa = 0.6$, respectively. Note again that these two curves do not represent quantitatively unambiguous solutions.

To understand why multiple solution sets occur for the absorptive regions of the 64 and 77% Cd samples, the uncertainty in theoretical transmission values must be examined with respect to variation in refractive index and uncertainty in sample layer thickness. The error in theoretical transmission, as compared with that measured, is a function of measured wavelength, measured layer thickness, and conjectured (by the algorithm) refractive index for that layer. Neglecting wavelength error, for a given wavelength value

$$\varepsilon_t(n, d) \equiv (T_T(n, d) - T_E)^2 \quad (12)$$

gives the transmission error ε_t in terms of the refractive index and the layer thickness; this is effectively the χ^2 value of a single data point as a function of n and d . To determine how rapidly the transmission error varies with layer thickness error, the function can be partially differentiated with respect to both parameters. While this analytical differentiation is prohibitively cumbersome, simple inferences can be made from the structure of transmission matrices. Because the propagation matrix contains β in the exponential of both diagonal terms, the partial derivative of ε_t will vary directly with n and d and will vary indirectly with λ . It is therefore expected that the transmission error will vary more rapidly in higher refractive index regions, thicker epitaxial films, and shorter-wavelength regions. The uncertainty in layer thicknesses measured by SIMS and RBS is known for all samples and is less than 10 nm in each case. Incidentally, not only are the refractive indices expected to be the highest for the 64 and 77% samples, but their layer thicknesses are also greater than those of the other four samples. Figure 6 shows two density plots depicting the transmission error for the 77% sample at different wavelengths as a function of layer thickness error (ε_d) and refractive index variation. The top image corresponds to $\lambda = 500$ nm and the bottom to $\lambda = 800$ nm. In the 500 nm transmission error plot there are two distinct, unconnected regions of minimum error, as enclosed by the dashed line. For $\lambda = 800$ nm of the same sample, there is only one such region and variation is slower, implying a smaller error value of the conjectured n itself for a given uncertainty in layer thickness. This degeneracy is seen in the 64 and 77% samples, but is not seen in any other sample. Such single-point degeneracy does not strictly imply solution degeneracy but with increased rate in error variation there is a decreased likelihood of reaching an optimal solution.⁴⁹

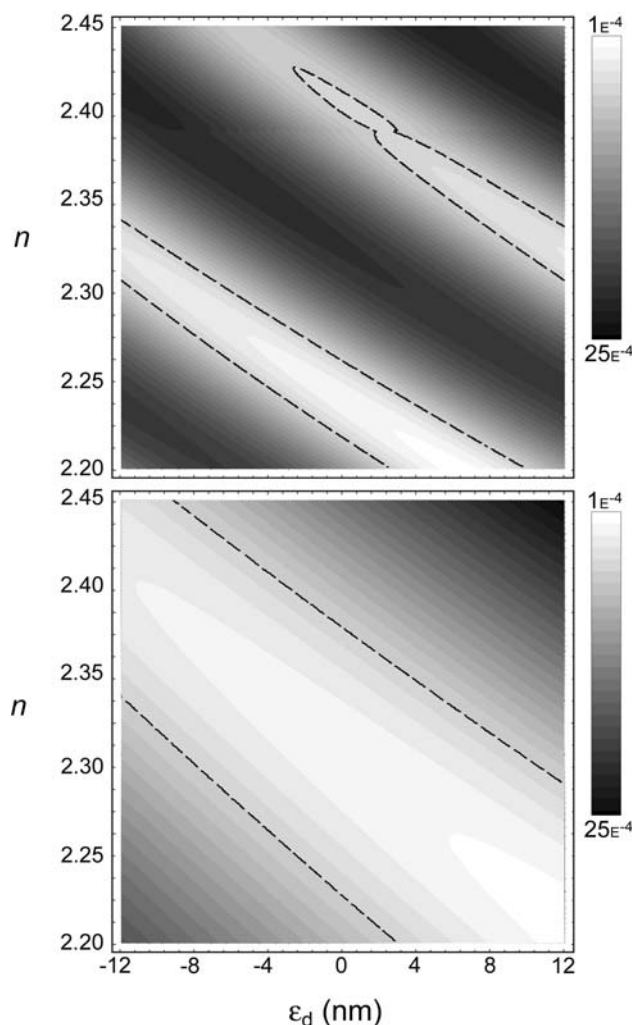


Fig. 6. Density plots showing the transmission error ε_t as a function of layer thickness error, and uncertainty in the initial guess of refractive index in our analysis for the 77% sample. The top figure shows ε_t at a wavelength of 500 nm and the bottom figure shows ε_t at a wavelength of 800 nm. The dashed lines correspond to the $\chi^2 = 5 \times 10^{-4}$ case, which specifies the neighborhood of least error in parameter space.

Ellipsometry

The result of the ellipsometry data fit for the $\text{Cd}_x\text{Zn}_{1-x}\text{O}$ layer with 16% cadmium concentration is shown in Fig. 7. It is observed that from around 470 nm to 1.8 μm the $\text{Cd}_{0.16}\text{Zn}_{0.84}\text{O}$ layer exhibits normal dispersion and is essentially transparent. The figure shows that the peak value of n occurs at 452 nm, which corresponds reasonably well with the spectrophotometric value of 442 nm. The n values at the peaks as determined by ellipsometry and spectrophotometry are 2.35 and 2.37, respectively. The Tauc-Lorentz model predicts a bandgap energy of 2.77 eV. In the region immediately below 449 nm it is found that the generalized oscillator model adequately fits the data. The bandgap transition is reasonably sharp, but not as sharp a transition as

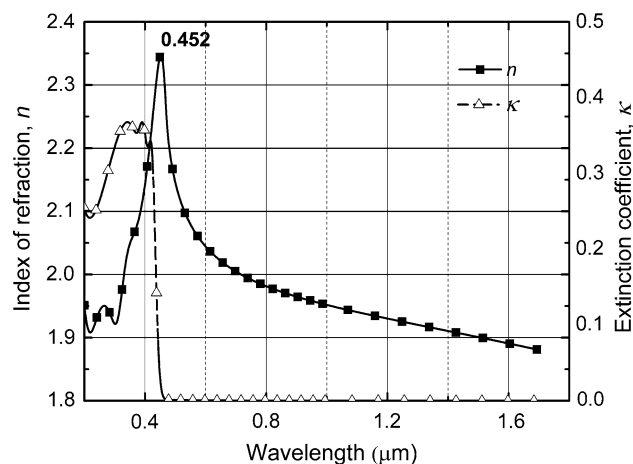


Fig. 7. Optical constants n and κ for the 16% $\text{Cd}_x\text{Zn}_{1-x}\text{O}$ sample as determined by spectroscopic ellipsometry. The peak in the refractive index curve occurs at 452 nm and is approximately 2.35.

that of the GaN sublayer, indicating the GaN layer may be more homogenous and have fewer crystal defects.

In the process of fitting, a correlation matrix is used to determine the minimum number of fitting parameters, and hence oscillators, needed to obtain the best fit. This procedure ensures the model is physically meaningful without introducing an excessive number of oscillators and fit parameters. The resulting physical interpretation is that $\text{Cd}_x\text{Zn}_{1-x}\text{O}$ has two small absorption peaks which overlap with the main bandgap transition peak. One shoulder occurs at 315 nm, and another, slightly broader shoulder, occurs at 236 nm. A strong pole at 11 eV out of the range of the plot to the left on Fig. 7 improves the fit and provides the residual accounting for $n(\infty)$. Oscillations in Ψ (interference fringes) due to interference between the air-to- $\text{Cd}_x\text{Zn}_{1-x}\text{O}$ and $\text{Cd}_x\text{Zn}_{1-x}\text{O}$ -GaN interfaces are symmetrical, indicating no measurable birefringence. A surface roughness layer and thickness nonuniformity options are allowed to fit in the model. We find that the top of the sample stack has an RMS surface layer roughness of 11 nm thick and average thickness nonuniformity of 1.76% for the $\text{Cd}_x\text{Zn}_{1-x}\text{O}$ layer. These options improve the model fit to account for depolarization effects.

Figure 8 shows the resulting curves for the refractive index fit for the 16% sample as obtained by ellipsometry, overlaid with that obtained by spectrophotometry. Good overall agreement is observed between both the real and imaginary refractive indices curves for the two techniques. An error analysis of the ellipsometry data revealed the standard deviations of the n and κ values to be $\sigma_n = \pm 0.013$ and $\sigma_\kappa = \pm 0.015$, respectively. Using a 2σ confidence interval to determine correlation between the fits, it was found that the n values are statistically well correlated at all points except for the range from 429 nm to 465 nm in which the

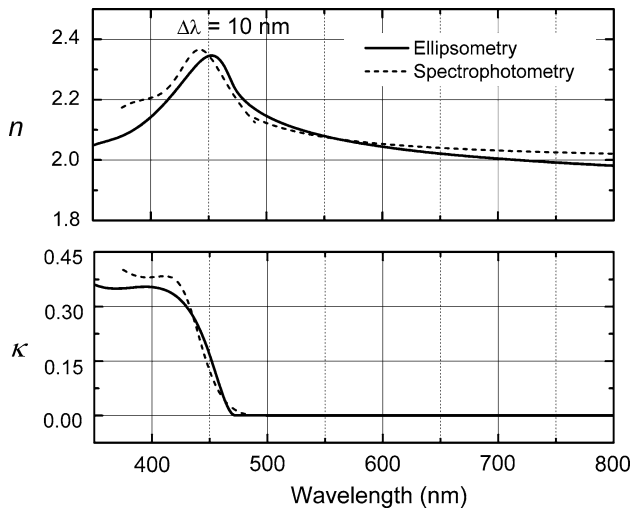


Fig. 8. The real (top) and imaginary (bottom) components of the refractive indices of the 16% sample as determined by spectrophotometry overlaid onto results obtained by spectroscopic ellipsometry showing good general agreement between the two techniques.

bandgap occurs. The peaks in the real refractive indices curves are separated by $\Delta\lambda = 10$ nm. The greater disagreement at the edges of the graph is due in part to the more limited range of the spectrophotometric data; however, the value for real refractive index at 800 nm differs between the two by only $\Delta n = 0.04$. The difference in slope in the transparent region is likely due to slight differences in the models used for underlying layers, including the GaN refractive index which is known to have some variation among the existing measurements.^{59–62} The absorption edges show similar slopes between the two curves and are in good agreement.

CONCLUSIONS

The complex refractive indices of wurtzite structure $\text{Cd}_x\text{Zn}_{1-x}\text{O}$ thin films were determined by fitting spectrophotometric transmission measurements to two optical dispersion models, the Sellmeier and Forouhi–Bloomer models. The cadmium concentrations of the epitaxial films used ranged from 2% to 77% and the spectral range of transmission measurements ranged from 375 nm to 800 nm. Spectroscopic ellipsometry was also carried out on one sample from 190 nm to 1.8 μm and fit to a generalized oscillator model. The real refractive indices of $\text{Cd}_x\text{Zn}_{1-x}\text{O}$ are seen to shift to higher values in the transparent region with increasing cadmium concentration while the dispersion bandgap parameter decreases in energy from 2.95 eV to 1.73 eV for 2 and 77% cadmium, respectively. Comparison between the spectrophotometry and ellipsometry methods confirms the validity of the use of spectrophotometry fitting for thin-film refractive index determination. Sources of algorithm-related errors are addressed.

ACKNOWLEDGEMENTS

The authors would like to acknowledge the support provided for this research through the Army Research Office (Contract # W911NF-05-C-0024), monitored by Dr. M. Gerhold. The authors would also like to thank Dr. I. Garibay for his help and guidance in the coding of the evolutionary algorithm, and express our gratitude to Mr. R. Synowicki of J.A. Woollam Co. for useful discussions on spectroscopic ellipsometry.

REFERENCES

1. G. Carlotti, G. Socino, and E. Verona, *Proc. of the IEEE Ultrasonics Symposium* (1988, vol. 1), 427 p.
2. V. Gulia and S. Kumar, *Opt. Mater.* 29, 778 (2007). doi:10.1016/j.optmat.2005.12.007.
3. H. Sasaki, K. Tsubouchi, N. Chubachi, and N. Mikoshiba, *J. Appl. Phys.* 47, 2046 (1976). doi:10.1063/1.322933.
4. T. Shiosaki and A. Kawabata, *Appl. Phys. Lett.* 25, 10 (1974). doi:10.1063/1.1655257.
5. J. Dong, A. Osinsky, B. Hertog, A. Dabiran, P. Chow, Y. Heo, D. Norton, and S. Pearton, *J. Electron. Mater.* 34, 416 (2005). doi:10.1007/s11664-005-0121-6.
6. T. Gruber, C. Kirchner, R. Kling, F. Reuss, and A. Waag, *Appl. Phys. Lett.* 84, 5359 (2004). doi:10.1063/1.1767273.
7. K. Koike, K. Hama, I. Nakashima, S. Sasa, M. Inoue, and M. Yano, *Jpn. J. Appl. Phys.* 1 44, 3822 (2005).
8. A. Osinsky, J. Dong, J.Q. Xie, B. Hertog, A. Dabiran, P.P. Chow, S.J. Pearton, D.P. Norton, D.C. Look, W.V. Schoenfeld, O. Lopatiuk, L. Chernyak, M. Cheung, A.N. Cartwright, and M. Gerhold, *MRS Symp. Proc.* 892, 429 (2006).
9. S. Sadofev, S. Blumstengel, J. Cui, J. Puls, S. Rogaschewski, P. Schafer, and F. Henneberger, *Appl. Phys. Lett.* 89, 201907 (2006). doi:10.1063/1.2388250.
10. D.C. Look, *Mater. Sci. Eng. B-Solid* 80, 383 (2001).
11. U. Ozgur, Y.I. Alivov, C. Liu, A. Teke, M.A. Reshchikov, S. Dogan, V. Avrutin, S.J. Cho, and H. Morkoc, *J. Appl. Phys.* 98, 1 (2005). doi:10.1063/1.1992666.
12. S. Nakamura, M. Senoh, S. Nagahama, N. Iwasa, T. Yamada, T. Matsushita, H. Kiyoku, and Y. Sugimoto, *Jpn. J. Appl. Phys.* 2 35, L74 (1996).
13. J.W. Orton and C.T. Foxon, *Rep. Prog. Phys.* 61, 1 (1998). doi:10.1088/0034-4885/61/1/001.
14. D.C. Look, D.C. Reynolds, J.R. Sizelove, R.L. Jones, C.W. Litton, G. Cantwell, and W.C. Harsch, *Solid State Commun.* 105, 399 (1998). doi:10.1016/S0038-1098(97)10145-4.
15. J.-J. Chen, F. Ren, D.P. Norton, S.J. Pearton, A. Osinsky, J.W. Dong, and S.N.G. Chu, *Electrochem. Solid St.* 8, G359 (2005). doi:10.1149/1.2119447.
16. N.B. Chen and C.H. Sui, *Mater. Sci. Eng. B-Solid* 126, 16 (2006).
17. T.S. Jeong, M.S. Han, J.H. Kim, S.J. Bae, and C.J. Youn, *J. Phys. D Appl. Phys.* 40, 370 (2007). doi:10.1088/0022-3727/40/2/013.
18. T. Makino, Y. Segawa, M. Kawasaki, A. Ohtomo, R. Shiroki, K. Tamura, T. Yasuda, and H. Koinuma, *Appl. Phys. Lett.* 78, 1237 (2001). doi:10.1063/1.1350632.
19. M.R.J.K.R. Thangavel, *Phys. Status Solidi B* 244, 3183 (2007). doi:10.1002/pssb.200743097.
20. Y.R. Ryu, T.S. Lee, J.A. Lubguban, A.B. Corman, H.W. White, J.H. Leem, M.S. Han, Y.S. Park, C.J. Youn, and W.J. Kim, *Appl. Phys. Lett.* 88, 052103 (2006). doi:10.1063/1.2168040.
21. T. Gruber, C. Kirchner, R. Kling, F. Reuss, A. Waag, F. Bertram, D. Forster, J. Christen, and M. Schreck, *Appl. Phys. Lett.* 83, 3290 (2003). doi:10.1063/1.1620674.
22. X.J. Wang, I.A. Buyanova, W.M. Chen, M. Izadifard, S. Rawal, D.P. Norton, S.J. Pearton, A. Osinsky, J.W. Dong, and A. Dabiran, *Appl. Phys. Lett.* 89, 151909 (2006). doi:10.1063/1.2361081.

23. K. Postava, H. Sueki, M. Aoyama, T. Yamaguchi, C. Ino, Y. Igasaki, and M. Horie, *J. Appl. Phys.* 87, 7820 (2000). doi:[10.1063/1.373461](https://doi.org/10.1063/1.373461).
24. X.W. Sun and H.S. Kwok, *J. Appl. Phys.* 86, 408 (1999). doi:[10.1063/1.370744](https://doi.org/10.1063/1.370744).
25. C.W. Teng, J.F. Muth, U. Ozgur, M.J. Bergmann, H.O. Everitt, A.K. Sharma, C. Jin, and J. Narayan, *Appl. Phys. Lett.* 76, 979 (2000). doi:[10.1063/1.125912](https://doi.org/10.1063/1.125912).
26. C. Bundesmann, A. Rahm, M. Lorenz, M. Grundmann, and M. Schubert, *J. Appl. Phys.* 99, 113504 (2006). doi:[10.1063/1.2200447](https://doi.org/10.1063/1.2200447).
27. N.B. Chen, H.Z. Wu, and T.N. Xu, *J. Appl. Phys.* 97, 023515 (2005). doi:[10.1063/1.1821633](https://doi.org/10.1063/1.1821633).
28. R. Schmidt, B. Rheinlander, M. Schubert, D. Spemann, T. Butz, J. Lenzer, E.M. Kaidashev, M. Lorenz, A. Rahm, H.C. Semmelhack, and M. Grundmann, *Appl. Phys. Lett.* 82, 2260 (2003). doi:[10.1063/1.1565185](https://doi.org/10.1063/1.1565185).
29. R. Schmidt-Grund, A. Carstens, B. Rheinlander, D. Spemann, H. Hochmut, G. Zimmermann, M. Lorenz, and M. Grundmann, *J. Appl. Phys.* 99, 123701 (2006). doi:[10.1063/1.2205350](https://doi.org/10.1063/1.2205350).
30. R. Schmidt-Grund, M. Schubert, B. Rheinlander, D. Fritsch, H. Schmidt, E.M. Kaidashev, M. Lorenz, C.M. Herzinger, and M. Grundmann, *Thin Solid Films* 455–456, 500 (2004). doi:[10.1016/j.tsf.2003.11.249](https://doi.org/10.1016/j.tsf.2003.11.249).
31. D.J. Channin, J.M. Hammer, and M.T. Duffy, *Appl. Opt.* 14, 923 (1975).
32. E.J. Ibang, C. Le Luyer, and J. Mugnier, *Mater. Chem. Phys.* 80, 490 (2003). doi:[10.1016/S0254-0584\(02\)00552-7](https://doi.org/10.1016/S0254-0584(02)00552-7).
33. C.L. Jia, K.M. Wang, X.L. Wang, X.J. Zhang, and F. Lu, *Opt. Exp.* 13, 5093 (2005). doi:[10.1364/OPEX.13.005093](https://doi.org/10.1364/OPEX.13.005093).
34. M.H. Koch, P.Y. Timbrell, and R.N. Lamb, *Semicond. Sci. Tech.* 10, 1523 (1995). doi:[10.1088/0268-1242/10/11/015](https://doi.org/10.1088/0268-1242/10/11/015).
35. K. Ellmer, *J. Phys. D Appl. Phys.* 34, 3097 (2001). doi:[10.1088/0022-3727/34/21/301](https://doi.org/10.1088/0022-3727/34/21/301).
36. J.H. Lee, K.H. Ko, and B.O. Park, *J. Cryst. Growth* 247, 119 (2003). doi:[10.1016/S0022-0248\(02\)01907-3](https://doi.org/10.1016/S0022-0248(02)01907-3).
37. X. Wu, T.J. Coutts, and W.P. Mulligan, *J. Vac. Sci. Technol. A* 15, 1057 (1997). doi:[10.1116/1.580429](https://doi.org/10.1116/1.580429).
38. Y.S. Park, C.W. Litton, T.C. Collins, and D.C. Reynolds, *Phys. Rev.* 143, 512 (1966). doi:[10.1103/PhysRev.143.512](https://doi.org/10.1103/PhysRev.143.512).
39. D.C. Reynolds and T.C. Collins, *Phys. Rev.* 185, 1099 (1969). doi:[10.1103/PhysRev.185.1099](https://doi.org/10.1103/PhysRev.185.1099).
40. H.D. Li, S.F. Yu, S.P. Lau, E.S.P. Leong, H.Y. Yang, T.P. Chen, A.P. Abiyasa, and C.Y. Ng, *Adv. Mater.* 18, 771 (2006). doi:[10.1002/adma.200501693](https://doi.org/10.1002/adma.200501693).
41. S.K. Hong, H.J. Ko, Y. Chen, T. Hanada, and T. Yao, *J. Vac. Sci. Technol. B* 18, 2313 (2000). doi:[10.1116/1.1303809](https://doi.org/10.1116/1.1303809).
42. A. Nakamura, J. Ishihara, S. Shigemori, K. Yamamoto, T. Aoki, H. Gotoh, and J. Temmyo, *Jpn. J. Appl. Phys.* 2 43, L1452 (2004).
43. S. Shigemori, A. Nakamura, J. Ishihara, T. Aoki, and J. Temmyo, *Jpn. J. Appl. Phys.* 2 43, L1088 (2004).
44. C.W. Sun, P. Xin, C.Y. Ma, Z.W. Liu, Q.Y. Zhang, Y.Q. Wang, Z.J. Yin, S. Huang, and T. Chen, *Appl. Phys. Lett.* 89, 181923 (2006). doi:[10.1063/1.2378527](https://doi.org/10.1063/1.2378527).
45. Z. Ye, D. Ma, J. He, J. Huang, B. Zhao, X. Luo, and Z. Xu, *J. Cryst. Growth* 256, 78 (2003). doi:[10.1016/S0022-0248\(03\)01314-9](https://doi.org/10.1016/S0022-0248(03)01314-9).
46. S. Choopun, R.D. Vispute, W. Yang, R.P. Sharma, and T. Venkatesan, *Appl. Phys. Lett.* 80, 1529 (2002). doi:[10.1063/1.1456266](https://doi.org/10.1063/1.1456266).
47. J.W. Mares, F.R. Ruhge, A.V. Thompson, P.G. Kik, A. Osinsky, B. Hertog, A.M. Dabiran, P.P. Chow, and W.V. Schoenfeld, *Opt. Mater.* 30, 346 (2007). doi:[10.1016/j.optmat.2006.11.058](https://doi.org/10.1016/j.optmat.2006.11.058).
48. A.B. Djurusic, *Opt. Commun.* 151, 147 (1998). doi:[10.1016/S0030-4018\(98\)00122-9](https://doi.org/10.1016/S0030-4018(98)00122-9).
49. E. Eberbach, *Biosystems* 82, 1 (2005). doi:[10.1016/j.bio.systems.2005.05.006](https://doi.org/10.1016/j.bio.systems.2005.05.006).
50. S. Jurecka, M. Jurechova, and J. Mullerova, *Acta Phys. Slovaca.* 53, 215 (2003).
51. J.H. Holland, *J. Assoc. Comput. Mach.* 9, 297 (1962). doi:[10.1145/321127.321128](https://doi.org/10.1145/321127.321128).
52. I. Rechenberg, ed., *Cybernetic Solution Path of an Experimental Problem* (Farnborough: Royal Aircraft Establishment, 1965), Library Translation No. 1122.
53. A.R. Forouhi and I. Bloomer, *Phys. Rev. B* 34, 7018 (1986). doi:[10.1103/PhysRevB.34.7018](https://doi.org/10.1103/PhysRevB.34.7018).
54. A.R. Forouhi and I. Bloomer, *Phys. Rev. B* 38, 1865 (1988). doi:[10.1103/PhysRevB.38.1865](https://doi.org/10.1103/PhysRevB.38.1865).
55. D. Poelman and P.F. Smet, *J. Phys. D Appl. Phys.* 36, 1850 (2003). doi:[10.1088/0022-3727/36/15/316](https://doi.org/10.1088/0022-3727/36/15/316).
56. H.G. Tompkins and E.A. Irene, eds., *Handbook of Ellipsometry* (New York: William Andrew Publishing Inc., 2005).
57. H.G. Tompkins, S. Tasic, J. Baker, and D. Convey, *Surf. Interface Anal.* 29, 179 (2000). doi:[10.1002/\(SICI\)1096-9918\(200003\)29:3<179::AID-SIA701>3.0.CO;2-O](https://doi.org/10.1002/(SICI)1096-9918(200003)29:3<179::AID-SIA701>3.0.CO;2-O).
58. J.A. Woollam, B. Johs, C.M. Herzinger, J. Hilfiker, R. Synowicki, and C.L. Bungay, *Proc. SPIE* CR72, 29 (1999).
59. N. Antoine-Vincent, F. Natali, M. Mihailovic, A. Vasson, J. Leymarie, P. Disseix, D. Byrne, F. Semon, and J. Massies, *J. Appl. Phys.* 93, 5222 (2003). doi:[10.1063/1.1563293](https://doi.org/10.1063/1.1563293).
60. M.J. Bergmann, U. Ozgur, J.H.C. Casey, H.O. Everitt, and J.F. Muth, *Appl. Phys. Lett.* 75, 67 (1999). doi:[10.1063/1.124278](https://doi.org/10.1063/1.124278).
61. A.B. Djurusic and E.H. Li, *J. Appl. Phys.* 89, 273 (2001). doi:[10.1063/1.1331069](https://doi.org/10.1063/1.1331069).
62. U. Ozgur and G. Webb-Wood, *Appl. Phys. Lett.* 79, 4103 (2001). doi:[10.1063/1.1426270](https://doi.org/10.1063/1.1426270).